CHAPTER IV: Structure and Magnetic Properties of $Ti_{1-x}Co_xO_2$ Nanoparticles and Nanowires

In this chapter, we have discussed the structural and magnetic properties of $Ti_{1-x}Co_xO_2$ nanoparticles as well as nanowires. Section 4.1 accounts for the structural phase transformation in TiO_2 nanoparticles synthesised at pH 4.5 and 6.5. Section 4.2 deals with the structural and magnetic properties of $Ti_{1-x}Co_xO_2$. The microstructure, magnetic properties and charge density distribution study of TiO_2 nanoparticles as well as nanowires synthesised by two step hydrothermal technique are discussed in Section 4.3. Charge density distribution studies have been undertaken using Maximum Entropy Method (MEM) using XRD tools. The results are summarized in Section 4.4.

4.1 Structural Phase Transition in TiO_2 Nanoparticles

Here we discuss the structural phase transformations of two sets of TiO_2 nanoparticles synthesised by sol-gel technique at pH 4.5 and 6.5 and calcined at different temperatures. Structural characterisations have been carried out using XRD, Raman and FT-IR. The microstructural and chemical analysis has been carried out using a TEM and XPS, respectively.

4.1.1 Structural Properties

TiO_2 nanoparticles synthesised via sol-gel technique at pH 4.5 and 6.5 are termed as sample A and B, respectively. The detailed technique has been given in Chapter III. The as synthesised sample A and B are calcined at 300, 500, 650, 800 and 850 ^oC. For simplicity, these samples are named as A-300, A-500, A-800, A-850, B-300, B-500, B-650 and B-800 hereafter.

TiO_2 samples synthesised at pH of precipitation 4.5 and 6.5 are amorphous in nature. Fig.4.1 (a) depicts the XRD patterns of sample A calcined at different temperatures. The amorphous to crystalline transformation initiates at 300 ^oC. The broad XRD peaks indicate the particles are of nano size. At 500 ^oC, each peak is well resolved and the XRD pattern is in excellent agreement with the reference pattern (JCPDS 21-1272) corresponding to the anatase phase of TiO_2. Fig.4.1 (b) shows the XRD pattern of sample B calcined at 500 ^oC and above. From Fig.4.1 (a) and (b), it is clear that both sample A

and B calcined at 500 ^{o}C show anatase phase. However, sample B shows a complete rutile phase and sample A demonstrates a mixture of anatase plus rutile phase after calcining at 800 ^{o}C. At 850 ^{o}C, sample A converts to the rutile phase completely whereas at 650 ^{o}C, sample B shows a dominant rutile phase. To confirm the structural properties, we have carried out Raman spectroscopic measurements of these nanoparticles.

Fig.4.2 (a) and (b) show the Raman spectra of sample A and B calcined at various temperatures. Factor group analysis reveals six Raman active modes such as one A_{1g}, two B_{1g} and three E_g modes for anatase, and four active modes such as A_{1g}, B_{1g}, B_{2g} and E_g mode for rutile. The modes observed in A-300, B-300 and A-500, B-500 are in good agreement with anatase structure of TiO_2 as reported by Ohsaka et al. (1978). However, the Raman modes corresponding to the sample calcined at 300 ^{o}C are relatively broader as compared to the sample calcined at 500 ^{o}C. It suggests the growth of the grains with increasing calcination temperature. The low frequency, E_g mode, observed at 145 cm^{-1} and 143 cm^{-1}, respectively, for samples A-500 and B-500 resembles the E_g mode at 144 cm^{-1} of TiO_2 single crystal [Ohsaka et al. (1978); Porto et al. (1967)]. Compared with sample A-300, this mode appears to be sharper in case of sample A-500 and B-500, indicating the enhancement of crystallinity with increasing calcination temperature that corroborates the XRD results. Four modes have been observed for sample A-800, A-850, B-650 and B-800, which match well with the rutile structure of TiO_2 [Chaves (1974)]. However, the low frequency B_{1g} mode occurring at ~143-145 cm^{-1} is somewhat of higher intensity for A-800 and B-650 compared with the pure rutile form as observed in case of A-850 and B-800. This indicates the presence of a small fraction of the anatase phase in A-800 as well as B-650 [Clegg et al. (2001); Melendres et al. (1989)]. The observation of the anatase phase in addition to the rutile phase in sample A-800 and B-650 further supports the XRD data.
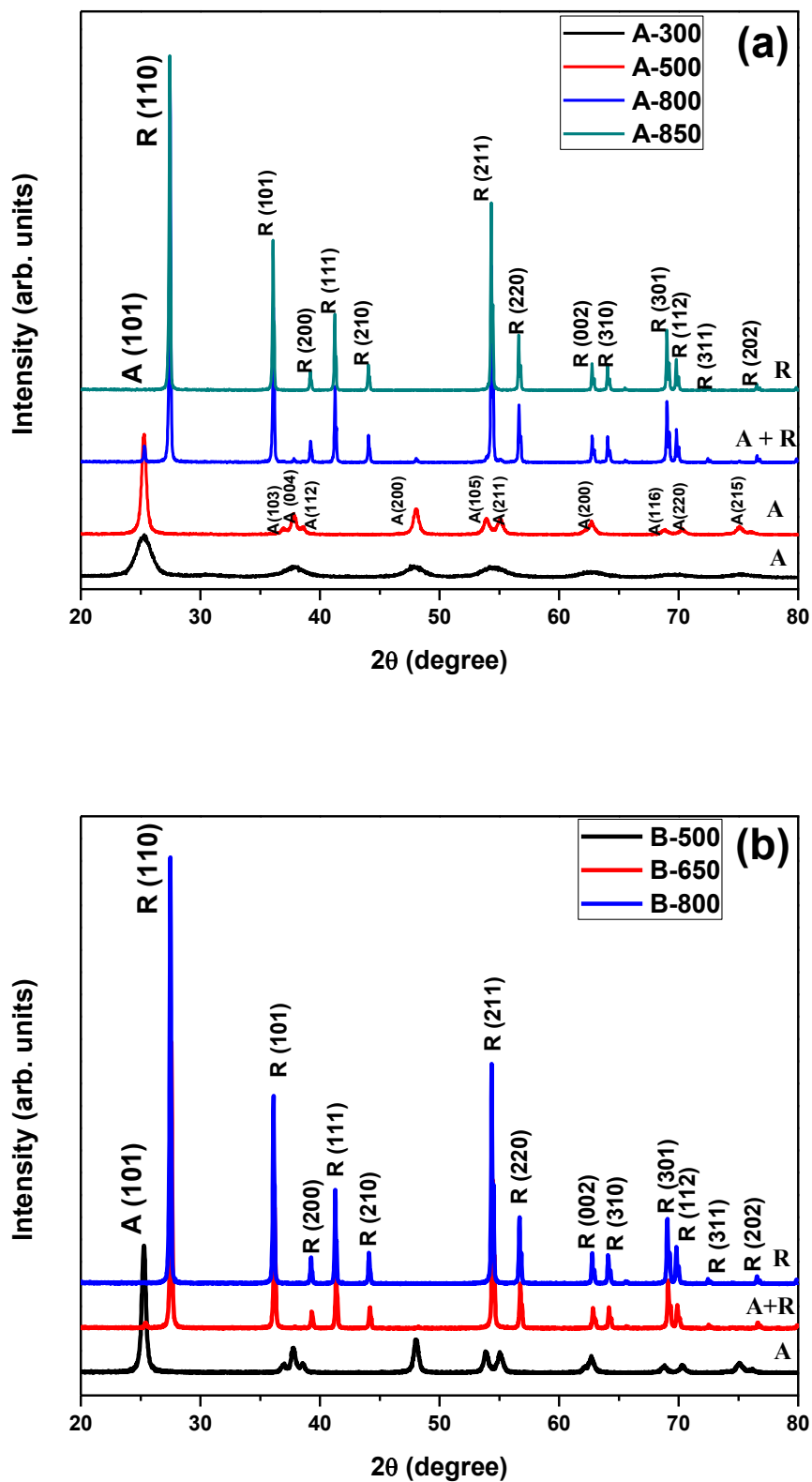
Fig.4.1 XRD patterns of TiO$_2$ nanoparticles synthesised at (a) pH = 4.5 (sample A), and (b) pH = 6.5 (sample B) calcined at different temperatures.
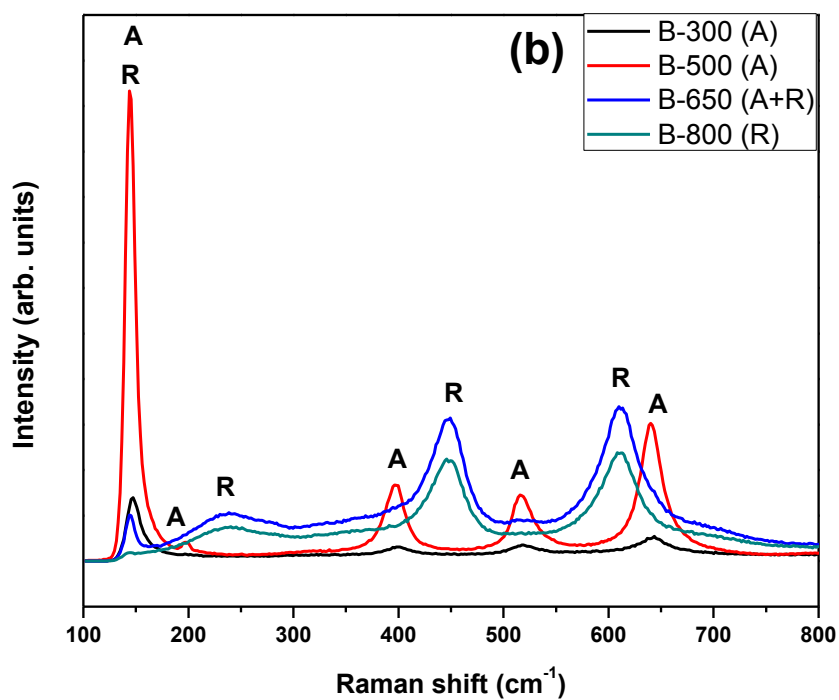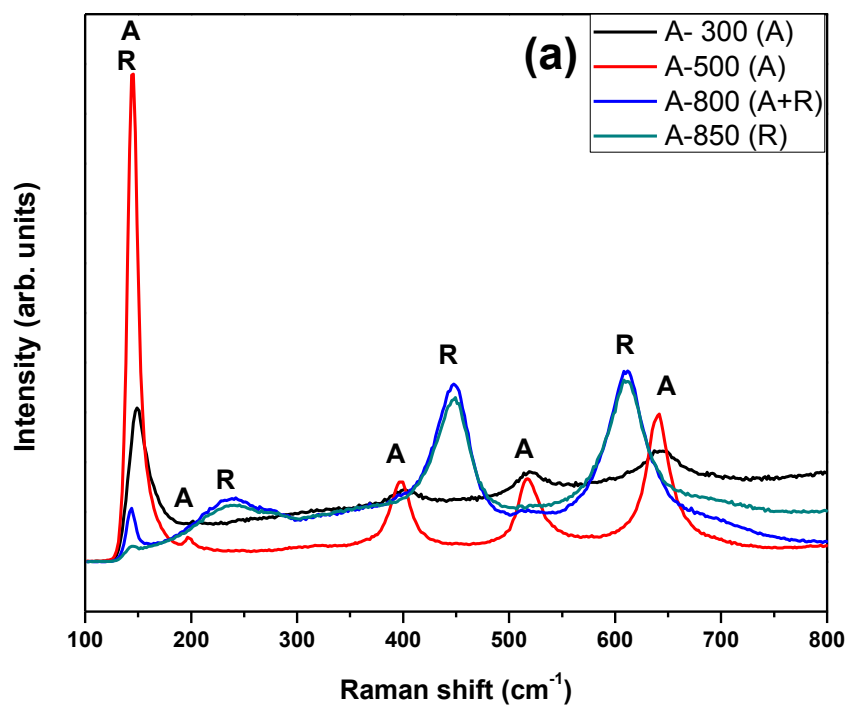
Fig.4.2 Raman spectra of (a) sample A and (b) sample B calcined at different temperatures.

The relative weight fractions of anatase phase (W_A) and rutile phase (W_R) for samples A-800 and B-650 are calculated using the relative intensity of the (1 0 1) peak of anatase (I_A) as well as the (1 1 0) peak of rutile (I_R) using the relationship proposed by Spurr and Myers (1957):

$$W_R = \frac{1}{1 + 0.8\frac{I_A}{I_R}} \dots \dots \dots \dots . (4.1)$$

$$W_A = \frac{1}{1 + 1.26\frac{I_R}{I_A}} \dots \dots \dots \dots . (4.2)$$

Using the above relation we have observed that while 99% of the anatase phase has converted to rutile in the case of B-650, 97% of the anatase phase has been transformed to the rutile phase for A-800. It is noteworthy to mention here that although the samples prepared at two different *p*H of precipitation exhibit same anatase phase at 500 °C, conversion of anatase to the rutile phase takes place at two different calcination temperature. For instance, the lower *p*H sample converts completely from anatase to rutile phase at a comparatively high calcination temperature (850 °C), whereas the higher *p*H sample shows similar conversion at a much lower calcination temperature i.e. 650 °C. Such *p*H dependent anatase to rutile phase transformation has not been reported before. Numerous studies have already been undertaken to study the anatase to rutile transformation mechanism. However, there is no consensus in literature regarding the lowest temperature at which the anatase to rutile transformation occurs. For example, Heald and Weiss (1972) show that anatase to rutile transformation begins at 900 °C. Suzuki and Kotera (1962) observe the initiation of anatase to rutile transformation at 800 °C. Further, the transformation temperature is reduced to 750 °C by Arroyo et al. (2002). The lowest anatase to rutile transformation temperature reported till date is 700 °C by [Li et al. (2004)]. Compared to all these reports, we may confidently state that anatase to rutile phase transformation starts at temperature much below 650 °C in the present case. While structure of the samples calcined at 500 °C

are completely identical, the drastic change in the anatase to rutile transformation temperature in both samples is quite surprising.

We have further carried out Fourier transform of infrared spectroscopy (FT-IR) of the sample A-500 and B-500 (Fig.4.3). All spectra show modes of bending vibration of the OH group (denoted by 1), stretching vibration of the OH groups (denoted by 2) and Ti-O-Ti as well as Ti-O-O bonds between 450 and 800 cm^{-1} denoted by 3. The structure of the low energy region (450 and 800 cm^{-1}) is not well resolved, which is characteristic feature of the sol-gel titania [Sanchez et al. (1996)]. One strong peak observed at 2354 cm^{-1} in sample B-500 is almost absent in sample A-500. This mode has been attributed to the atmospeheric CO_2 [Sanchez et al. (1996)]. This peak has been reduced after calcining the sample at 650 ^{o}C (inset of Fig.4.3).
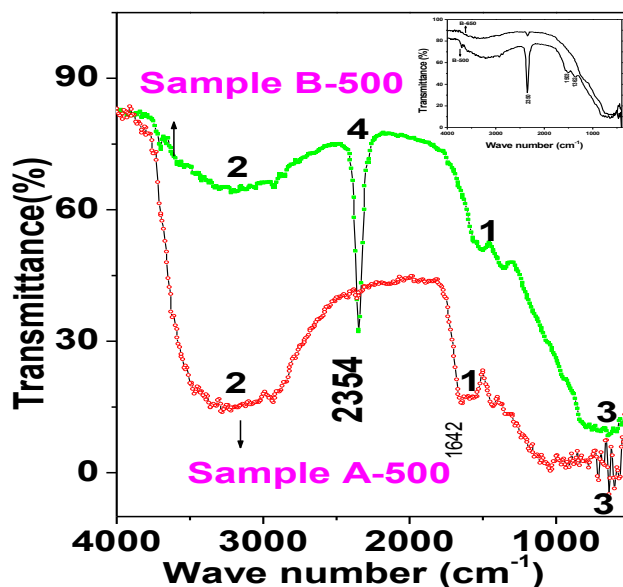

Fig.4.3 FT-IR of sample A-500 and B-500. Inset shows the comparison of samples B-500 with B-650.

4.1.2 TEM Results

To investigate the role of particle size on the anomaly in anatase to rutile phase transformation, we have carried out TEM measurements of sample A-

500 and B-500. Fig.4.4 (a) and (b) shows the transmission electron micrographs of A-500 and B-500, respectively. Though the size distribution is not uniform but it is evident that the particles are of nanosize (insets of Fig. 4.4). As the particle size is not very uniform, we calculate the size for several particles. We found that the particle size ranges from 18 nm to 25 nm and 25 nm to 35 nm in sample A-500 and B-500, respectively. Fig.4.4 (c) and (d) shows selected area electron diffraction (SAED) pattern of sample A-500 and B-500 respectively. The well-distinct ring patterns confirm the crystalline nature of the nanoparticles. Further, we have measured the crystallite sizes from the XRD line width using the Scherrer formula and are found to be 18 nm and 25 nm, respectively, for samples A-500 and B-500. The crystallite size obtained from the XRD line width matches well the particle size measured from the TEM.

4.1.3 XPS Results

To get qualitative information about the oxygen vacancies as well as oxidation states of the elements we have carried out XPS measurements. Fig.4.5 (a) shows the Ti core level spectra for sample A-500 and B-500. The core level binding energies of Ti $2p_{3/2}$ and Ti $2p_{1/2}$ are observed at 458.75 eV and 464.55 eV, respectively. The difference of 5.8 eV in both peaks indicates a valence state of +4 for Ti in both the samples [Murata et al. (1975)]. The normalized O 1s peak is shown in Fg.4.5 (b). The O 1s core levels show a slightly asymmetric shape around 530 eV and can be fitted well by two Gaussian curves which are denoted as Oa and Ob, respectively as shown in Fig.4.6. The Oa peak is ascribed to the oxygen atoms of TiO_2 whereas Ob peak is assigned to the hydroxyl groups, chemisorbed oxygen and organic oxygen on the surface of the sample [Kallel et al. (2009); Bessergenev et al. (2006)]. Naeem et al. (2006) have shown that the Ob peak is developed with increasing oxygen vacancies. Comparing the area ratio of Ob to Oa in samples A-500 and B- 500 (Fig.4.6 (a) and (b)), it is observed that the ratio is higher in the latter

than the former, indicating the enhancement of oxygen vacancy concentration [Zhao et al. (2007)].
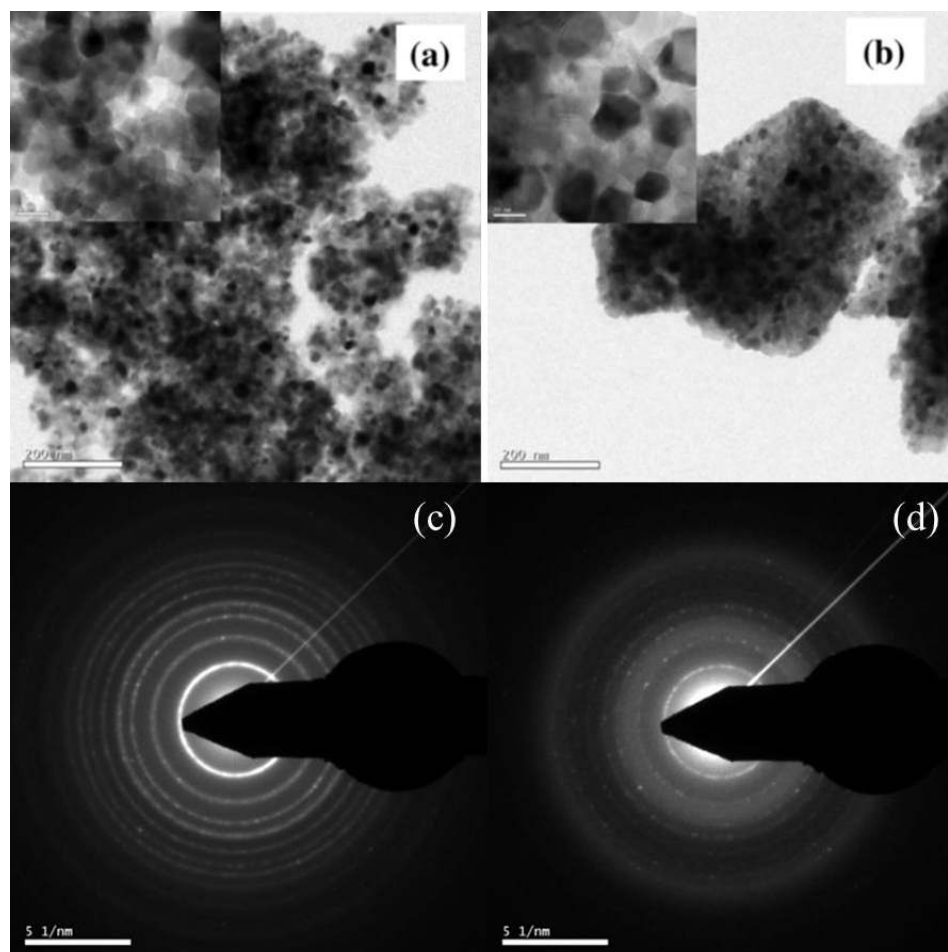

Fig.4.4 Transmission electron micrographs of (a) A-500 and (b) B-500 samples. SAED patterns of sample A-500 (c) and (d) and B-500.
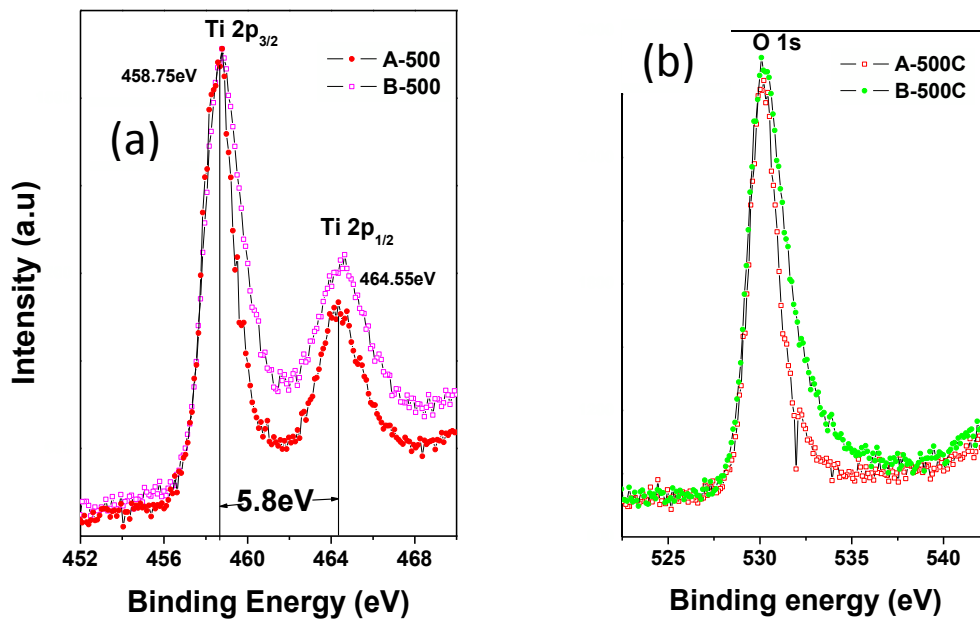
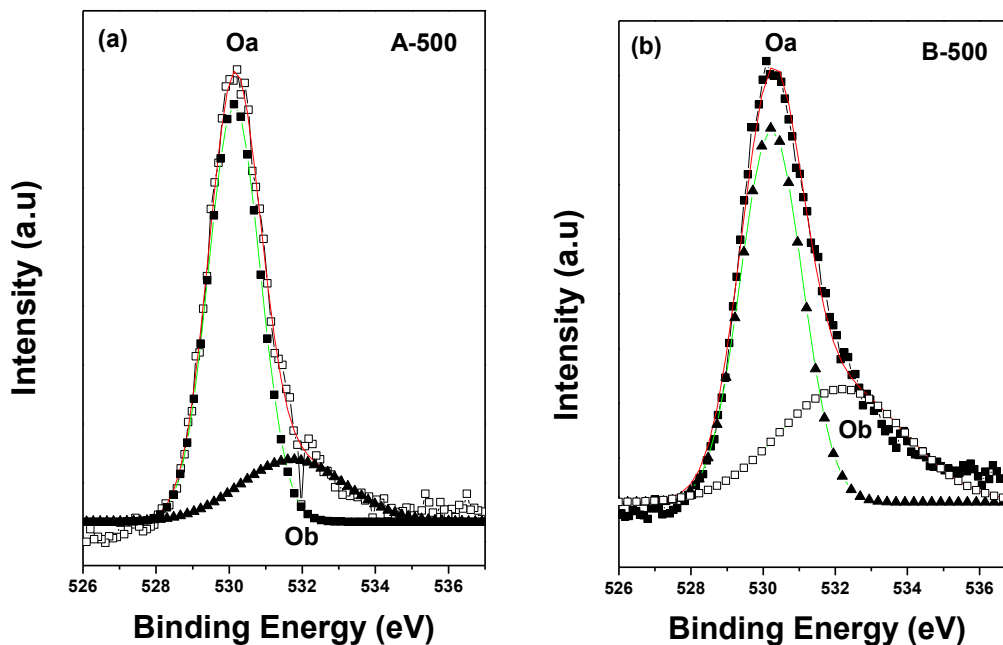**Fig.4.5** Normalized XPS spectra of samples A-500 and B-500: (a) Ti 2p core levels and (b) O 1s core level.

Fig.4.6 Deconvolution of O 1s core level: Oa and Ob peaks of A-500 and B-500 samples are shown in (a) and (b) respectively.

4.1.4 Discussion

The optical band gap energy (E_g) determined from the absorption coefficient "α" calculated as a function of the incident photon energy E (hv) yields 3.48 eV for A-500 and 3.22 eV for B-500. The optical band gap corroborates the crystallite size as obtained from the XRD. The smaller crystallite size of A-500 should show a lower anatase to rutile transformation temperature compared with B-500, which is opposite in our case. Li *et al* have shown 700 ^{o}C as the lowest anatase to rutile transformation temperature for the crystallite size of 13 nm [Li et al. (2004)]. However, even with a higher crystallite size (~25 nm), we have observed a lower anatase to rutile transformation temperature (650 ^{o}C). The other factor which affects the anatase to rutile transformation temperature is oxygen vacancy that can be controlled during particle growth [Zhao et al. (2006)]. These oxygen vacancies are also responsible for magnetic ordering in semiconductors. We have examined it in nanoparticles of TiO_2 in next section and in TiO_2 thin films in Chapter V.

The mechanism of anatase to rutile transformation is basically a nucleation and growth process. It is nucleated at the anatase {112} twin boundaries. Half of the titanium cations in the twin slab displace and the rutile phase nucleates [Li et al. (2004)]. The transformation of bulk anatase ruptures seven out of the twenty four Ti-O bonds per unit cell and leads to the cooperative displacement of both Ti and O. The transformation from anatase to rutile continues at the expense of destabilization of anatase octahedra. It has been reported that the fine crystallite size of the anatase phase enhances the nucleation sites and it is known that any increase in nucleation sites will favour the anatase to rutile transformation [Li et al. (2004)]. Reidy et al. (2006) have shown that by the addition of dopants such as Co, Mn and V to TiO_2, one may create defect sites which provide a low energy mass transport route and lower the anatase to rutile transformation temperature. Thus, higher is the oxygen vacancy, the lower is the anatase to rutile transformation temperature. Our results clearly envisage that instead of crystallite size, the surface

characteristics play an important role in deciding the temperature for anatase to rutile transformation. The larger oxygen vacancy concentration in sample B-500 compared with A-500 as observed from XPS lowers the anatase to rutile transformation temperature by providing a low energy mass transport route. Although XRD and Raman spectra are exactly the same in the samples prepared at two different *p*H of precipitation, XPS studies could genuinely distinguish the difference between them and also explain the origin of the lower anatase to rutile transformation temperature. Hence, oxygen vacancies are found to play a vital role in anatase to rutile phase transformation.

4.2. Structural and Magnetic Properties of $Ti_{1-x}Co_xO_2$ Nanoparticles

We have carried out that the structure dependent magnetic properties for TiO2 synthesised at *p*H 6.5 as it shows lower anatatse to rutile phase transformation and contains higher oxygen vacancies.

4.2.1 Structural Properties

$Ti_{1-x}Co_xO_2$ (x = 0.01, 0.03 and 0.05) nanoparticles have been synthesised by sol-gel technique at *p*H 6.5. The dried samples have been calcined at 500 °C. Fig.4.7 (a) depicts the XRD pattern of $Ti_{1-x}Co_xO_2$ (x = 0, 0.01, 0.03 and 0.05) calcined at 500 ^{o}C. The sample $Ti_{1-x}Co_xO_2$ with x = 0 is same as sample B-500 which has been discussed in the previous section. The XRD peaks are matched well with the reference pattern corresponding to anatase phase of TiO_2. Neither rutile, brookite phase nor any impurity phase have been observed within the detection limit of the XRD upto x = 0.03. A trace of $CoTiO_3$ secndary phase is detected for x =0.05 (Fig.4.7 (a)). Similar, precipitation of $CoTiO_3$ phase with increasing Co concentration in TiO_2 has been reported in literature [Li et al. (2009); Burdett et al. (1987)]. However, we do not observe
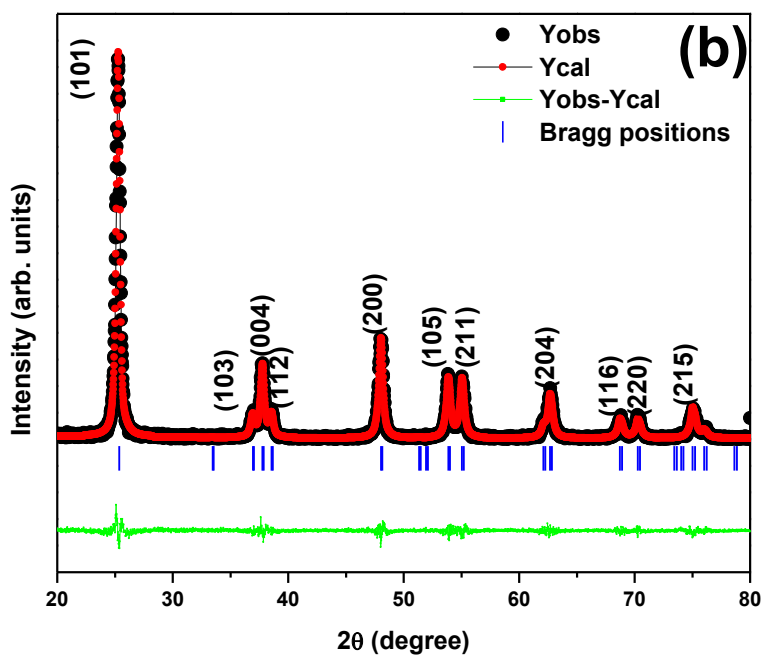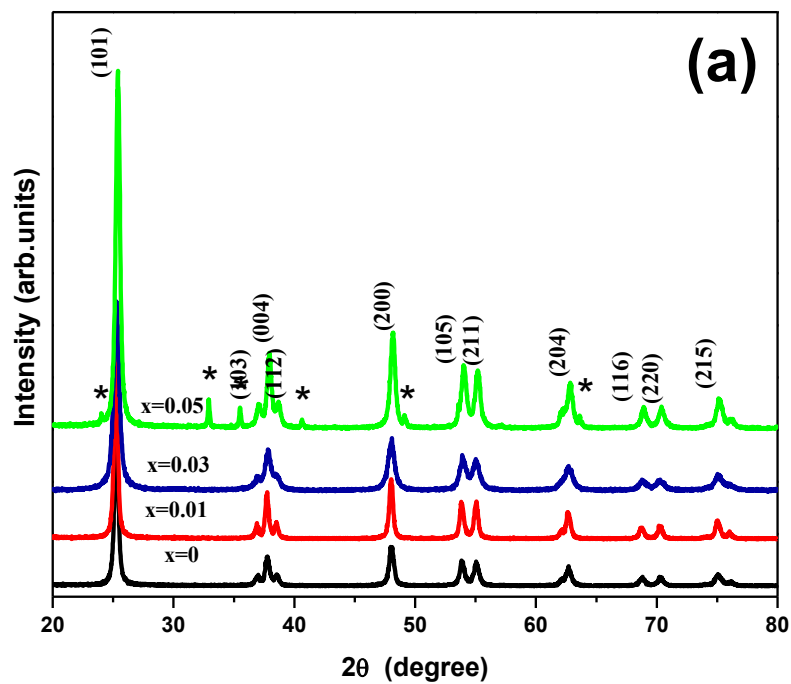
Fig.4.7 (a) XRD patterns of $Ti_{1-x}Co_xO_2$ (x = 0, 0.01, 0.03 and 0.05) synthesised at *p*H = 6.5 and calcined at 500 ^{o}C. (b)A typical Le-Bail profile fitting of TiO_2 (i.e., x = 0)

any anatase to rutile phase transformation with increasing cobalt concentration as observed by Reddy et al. (2007) and Barkat et al. (2005). The broad XRD peaks indicate smaller crystallite size of the samples. However, a trace of $CoTiO_3$ secondary phase has been seen for x = 0.05 (Fig.4.7 (a)). The XRD patterns of $Ti_{1-x}Co_xO_2$ are refined using the FullProf program considering I41/amd space group. A typical XRD spectrum for x = 0 after Le-Bail profile fitting is shown as Fig.4.7 (b). A good fit between the observed and the calculated profile is obtained as indicated from the flat difference profile. The lattice parameters and unit cell volume of the $Ti_{1-x}Co_xO_2$ (x = 0, 0.01, 0.03) after Le-Bail profile fitting are listed in Table 4.1.

Table 4.1: Lattice parameters and unit cell volume of $Ti_{1-x}Co_xO_2$ (x = 0, 0.01, 0.03).

$Ti_{1-x}Co_xO_2$	a (Å)	c (Å)	Lattice volume $(Å)^3$
x = 0	3.7855 ± 0.0001	9.5173 ± 0.0005	136.38 ± 0.01
x = 0.01	3.7868 ± 0.0001	9.5208 ± 0.0004	136.528 ± 0.009
x = 0.03	3.7869 ± 0.0002	9.5031 ± 0.0007	136.29 ± 0.01

The 'a' and 'c' parameters are matched well with the bulk value (a = 3.785 Å and c = 9.512 Å) [Manivannan et al. (2003)]. No significant change in lattice parameters is noticed upto x = 0.3 in agreement with the previous results [Ohshaka et al. (1978)]. To confirm the structural properties, we have carried out Raman spectroscopic measurements.

Fig.4.8 depicts the Raman spectra of $Ti_{1-x}Co_xO_2$ nanoparticles. Six allowed modes appear at 144 cm^{-1} (E_g), 197 cm^{-1}(E_g), 399 cm^{-1} (B_{1g}), 519 cm^{-1} (B_{1g}) and 639 cm^{-1}(E_g), which are in good agreement with the anatase structure of TiO_2 [16]. In addition to the above modes, for x = 0.05 two additional modes appear at 336 cm^{-1} and 695 cm^{-1}. These are corresponding to the ilmenite structure of $CoTiO_3$ (shown with '*' mark in the inset of the Fig.4.8) [Porkodi et al. (2007)]. The absence of 446 cm^{-1} and 609 cm^{-1} peak characteristics of the
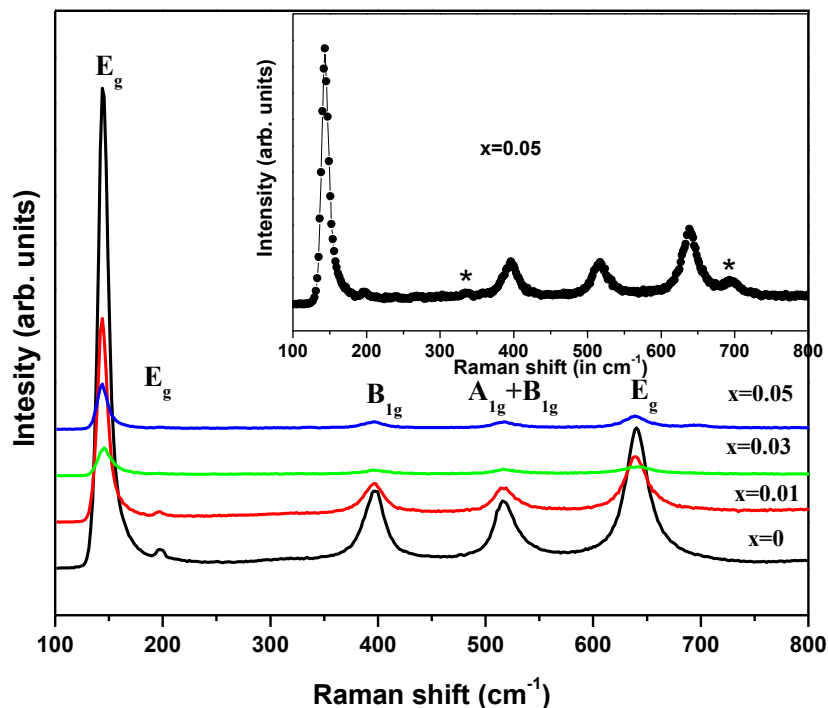
Fig.4.8 Raman spectra of $Ti_{1-x}Co_xO_2$ (x = 0, 0.01, 0.03 and 0.05) calcined at 500 °C.

rutile phase [Pradhan et al. (2005)], and absence of peak related to Co clusters or interstitials confirm the anatase phase upto x = 0.03 [Lisboa-Filho et al. (2002)]. Both the XRD and Raman studies confirm the anatase phase in x = 0 to 0.03 and a precipitation of $CoTiO_3$ secondary phase for x = 0.05. We have further carried out Fourier transform of infrared spectroscopy (FT-IR) of the samples $Ti_{1-x}Co_xO_2$ (Fig.4.9). All spectra show modes of bending vibration of the OH group (denoted by 1), stretching vibration of the OH groups (denoted by 2) and Ti-O-Ti as well as Ti-O-O bonds between 450 and 800 cm^{-1} as denoted by 3. The structure of the low energy region (450 and 800 cm^{-1}) is not well resolved, which is characteristic feature of the sol-gel titania [Sanchez et al. (1996)]. One strong peak observed at 2354 cm^{-1} for sample x = 0, is almost diminished for the other two samples. This mode has been attributed to the atmospheric CO_2 adsorbed over the sample surface [Sanchez et al. (1996)].
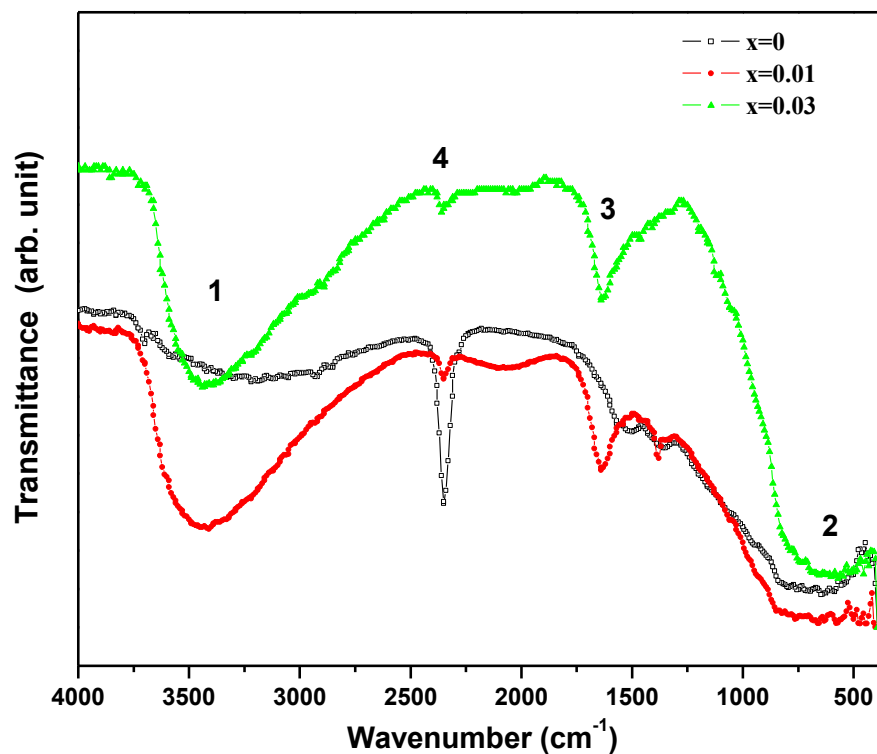
Fig.4.9 FT-IR spectra of $Ti_{1-x}Co_xO_2$ (x = 0, 0.01, 0.03) calcined at 500 ^{o}C.

4.2.2 Magnetic Properties

The magnetic properties of the nanoparticles, is studied using a PPMS-VSM (from Quantum Design, USA). DC Susceptibility (χ) as a function of temperature (T) for x = 0 to 0.03 are shown in Fig.4.10 (a). The temperature dependence of magnetisation shows identical behaviour under zero field cooling (ZFC) and field cooling (FC) conditions. For x = 0.05, with decreasing temperature from 300 K, we observe a paramagnetic to anti-ferromagnetic phase transition at 37 K which corresponds to the Neel temperature (T_N) of antiferromagnetic $CoTiO_3$ phase (shown as inset of Fig.4.10 (a)) [Coey et al. (2005)]. Hence, the presence of $CoTiO_3$ phase as predicted from the XRD and Raman results is also supported with the susceptibility measurement. One may note that the order of susceptibility of x = 0 at lowest temperature (Fig.4.10)

shows four and two fold increase in comparison to x = 0.01 and 0.03 respectively. The high temperature inverse susceptibility (χ) is fitted with the Curie-Weiss law:

$$\frac{1}{\chi} = \frac{T - \theta}{C} \ldots \ldots \ldots \ldots \ldots \ldots \ldots \ldots \ldots \ldots . (4.3)$$

where T is temperature, θ is Curie temperature and C is Curie constant. Fitting with Curie Weiss law, we found that the experimental curve deviates from the straight line at low temperature (Fig.4.10 (b)). By extrapolating, it cuts the –ve temperature axis confirms the presence of an anti-ferromagnetic ordering. Similar results have been previously reported by our group in Co-doped ZnO nanoparticles [Rath et al. (2009)]. Coey et al. (2005) have shown that ferromagnetism is more prominent in transition metal doped oxide semiconductors below a percolation limit and above it the ordering is dominated by the antiferromagnetic interaction. The percolation limit of Co at TiO_2 matrix is reported as x = 0.006 and beyond, the samples show a paramagnetic behaviour [Reddy et al. (2007)]. Samples with x = 0.01 and 0.03 are well above the percolation limit and hence are possibly not showing the ferromagnetic ordering. The enhancement of magnetic susceptibility is further examined by measuring the magnetisation with applied magnetic field. Magnetisation at maximum field (50 kOe) is also found to be higher in TiO_2 than Co-doped samples (Fig.4.11).
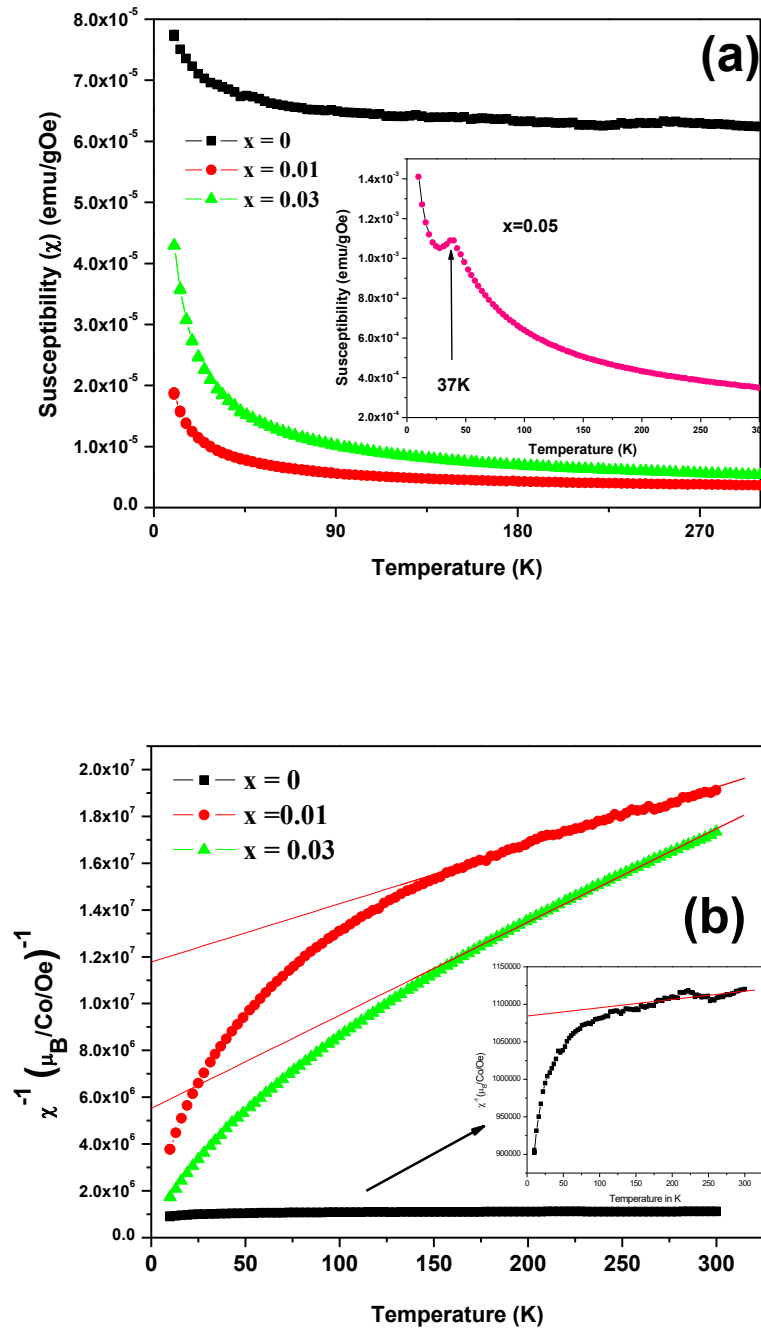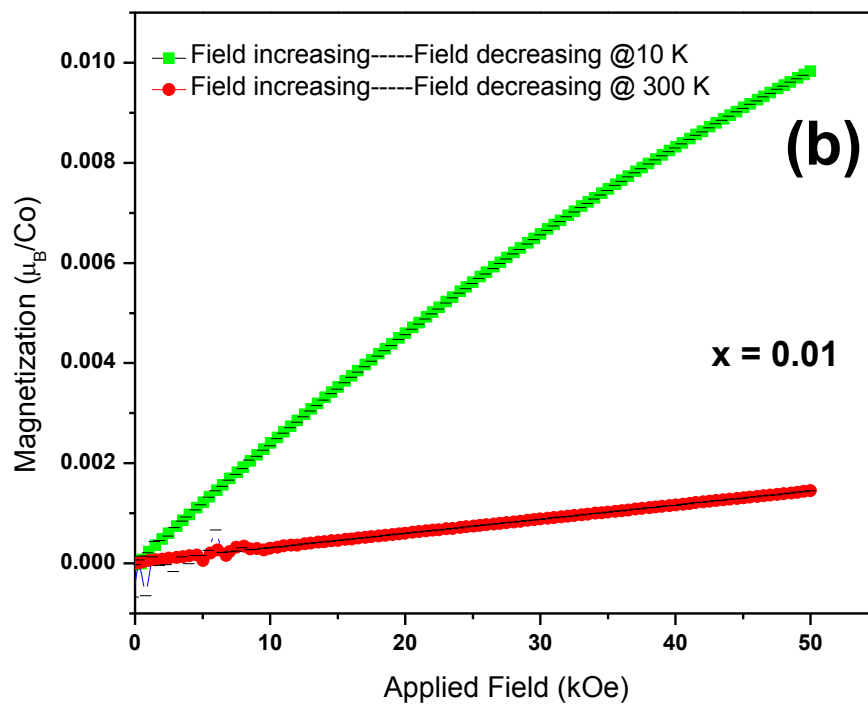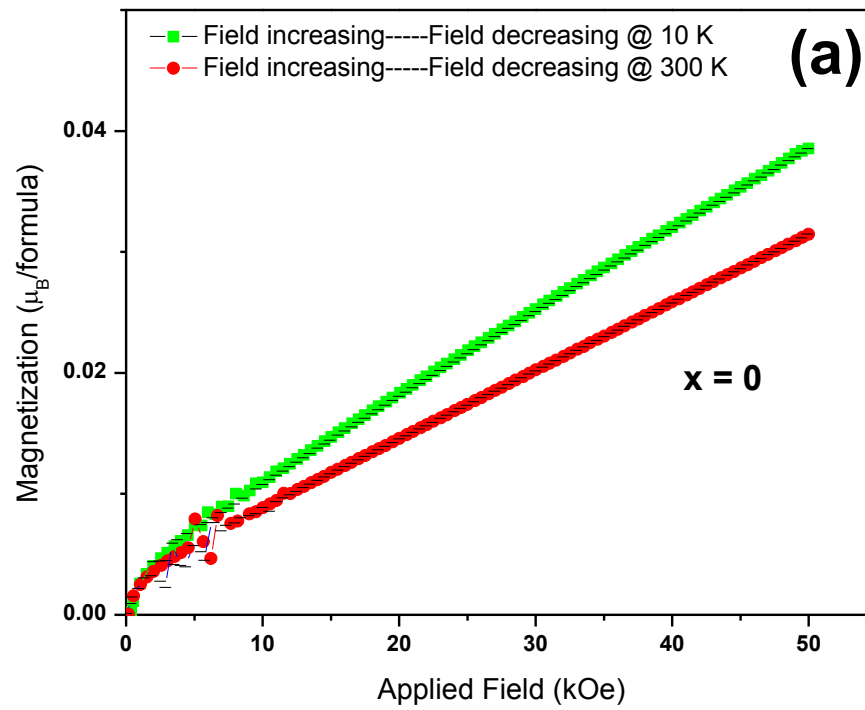
Fig.4.10 (a) Susceptibility as a function of temperature for $Ti_{1-x}Co_xO_2$ (x = 0, 0.01, 0.03) [inset shows the T_N of $CoTiO_3$] (b) Inverse susceptibility as a function of temperature for $Ti_{1-x}Co_xO_2$ (x = 0, 0.01, 0.03) [inset shows the zoomed in view for x = 0]
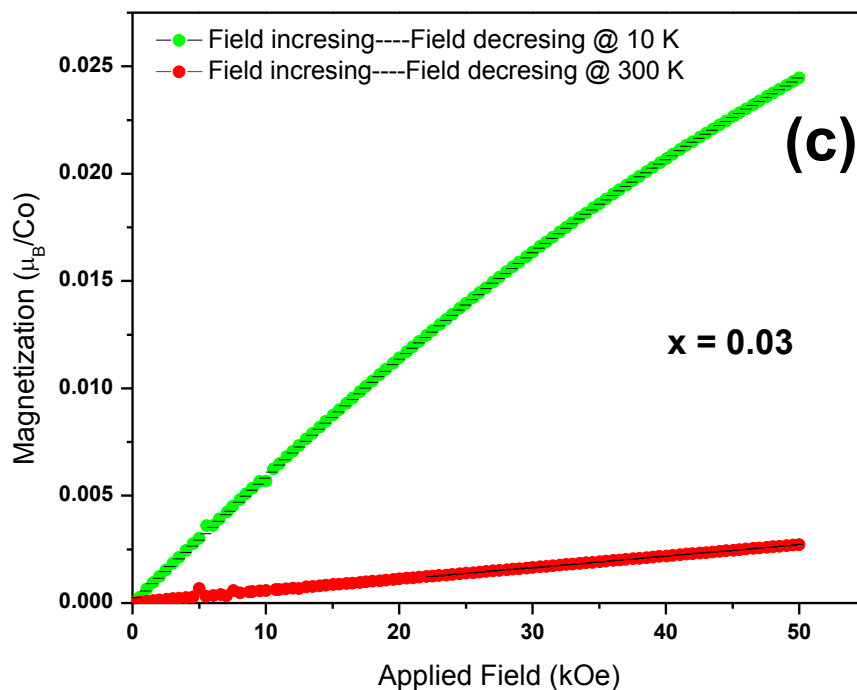
Fig.4.11 Magnetisation as a function of applied magnetic field for $Ti_{1-x}Co_xO_2$ for (a) x = 0, (b) x = 0.01 and (c) x = 0.03 measured at 10 and 300 K.

No hysteresis has been observed even at 10 K (Fig.4.11). Careful investigation of the M-H data for x = 0 at low field shows a non-linear behaviour indicating weak ferromagnetic like feature (Fig.4.11 (a)). The higher magnetic moment in undoped TiO_2 and appearance of nonlinearity in the M-H plot in comparison to Co doped samples is quite unexpected. To understand this anomaly, we have examined the role of size, valency of cations and oxygen vacancies.

4.2.3 Effect of Size

We have calculated the average crystallite size using the Sherrer formula [Cullity (1978)]. It is found to be of ~ 30 nm for both x = 0 and 0.01 samples and reduced by half in case of x = 0.03.
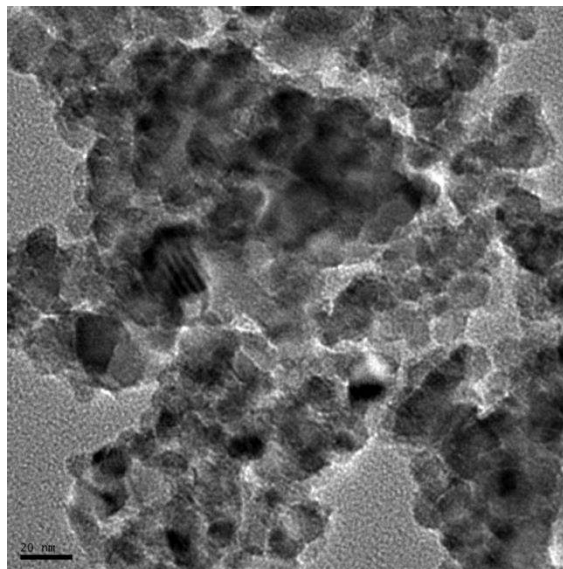
Fig.4.12 Transmission electron micrograph of $Ti_{0.97}Co_{0.03}O_2$ nanoparticles.

The particle size estimated from transmission electron micrographs are matched well with the crystallite size measured from the XRD line width. A typical TEM micrograph for sample having x = 0.03 is shown as Fig.4.12. Though there is no difference in size for x = 0 as well as x = 0.01, large change in magnetic properties is quite surprising. For x = 0.03, though magnetisation increases compared to x = 0.01, still it is less than x = 0 sample.

4.2.4 XPS Studies

The possible reason for higher magnetic moment in x = 0 could be due to generation of anion defects associated with the Ti^{3+} and/or Ti^{2+} or oxygen vacancies [Bessergenev et al. (2006); Naeem et al. (2006); Kallel et al. (2009)]. Typical XPS spectra for x = 0 and x = 0.03 are shown in Fig.4.13. The energy difference between the Ti core $2p_{3/2}$ level and $2p_{1/2}$ level is approximately 5.8 eV signifying Ti in 4+ valence state for both samples (Fig. 4.13 (a)). Fig.4.13 (b) shows the XPS spectra of the Co 2p level for x = 0.03. The binding energies 796.5 and 780.7eV respectively (Fig.4.13 (b)), for Co $2p_{3/2}$ and $2p_{1/2}$ states clearly rule out the presence of Co^{3+} ions. Being confirmed that Ti is in the +4 valence state and Co is in the +2 valance state, we proceed further to focus on the O 1s corelevel. The normalized O 1s peak is shown in Fig.4.13(c) (for x =

0, 0.03). The O 1s core level shows slightly asymmetric shape around 530 eV and can be well fitted by two Gaussian curves which are denoted as $Oa_{1/2}$ and $Ob_{1/2}$ (subscript 1 for x = 0 and 2 for x = 0.03) peaks respectively. The $Oa_{1/2}$ peak is ascribed to the lattice oxygen atoms of TiO_2 [Bessergenev et al. (2006)]. The $Ob_{1/2}$ component is assigned to hydroxyl groups, chemisorbed oxygen and organic oxygen on the surface of the sample [Kallel et al. (2009)]. Comparing the area ratio of $Ob_{1/2}$ to that of $Oa_{1/2}$ in case of x = 0 and x = 0.03, it is observed that the area ratio is higher in case of x = 0 than that of x = 0.03 indicating higher oxygen vacancies in the former [Naeem et al. (2006)]. Li et al. (2009) have shown that in bulk Co-doped TiO_2, oxygen vacancies are generally created after doping cobalt in place of Ti and magnetic moment increases. However, in the present case, large numbers of intrinsic oxygen vacancies available in TiO_2 are being compensated upon Co substitution and decrease the net magnetic moment in x = 0 and 0.03. Thus, oxygen vacancies are not only found to lower the anatase to rutile phase transformation temperature but also induce higher magnetic moment in TiO_2 nanoparticles.
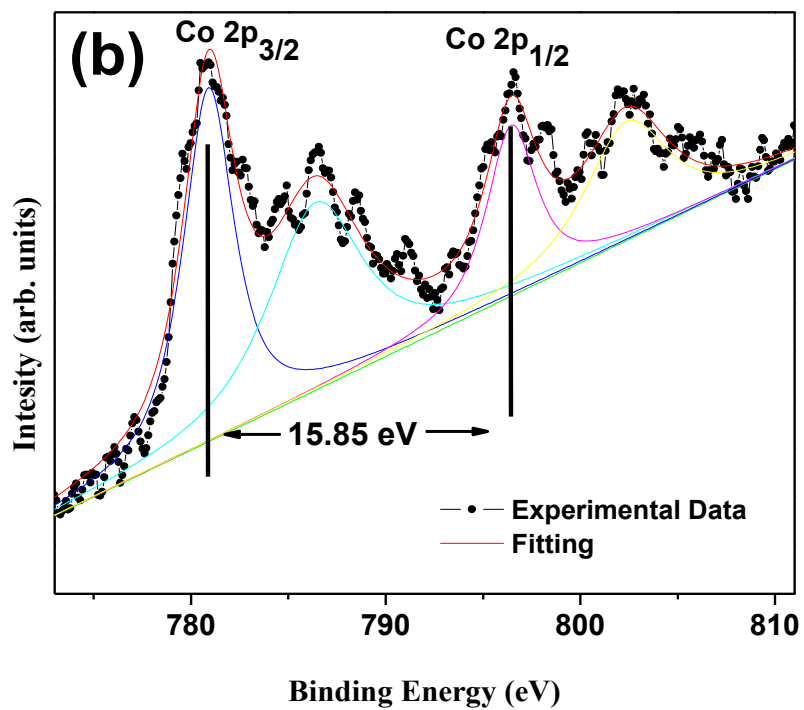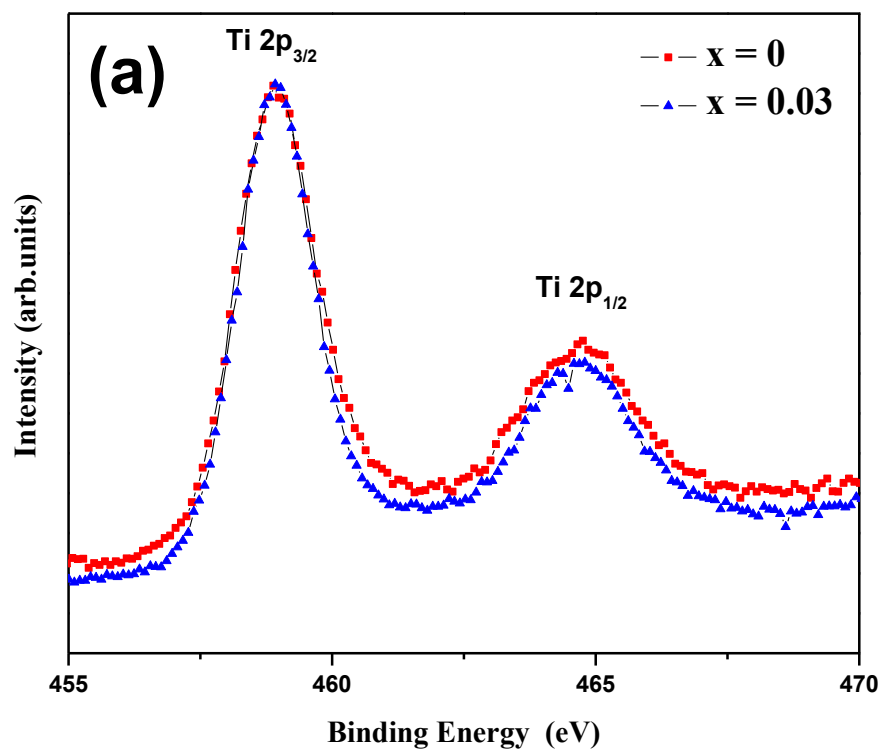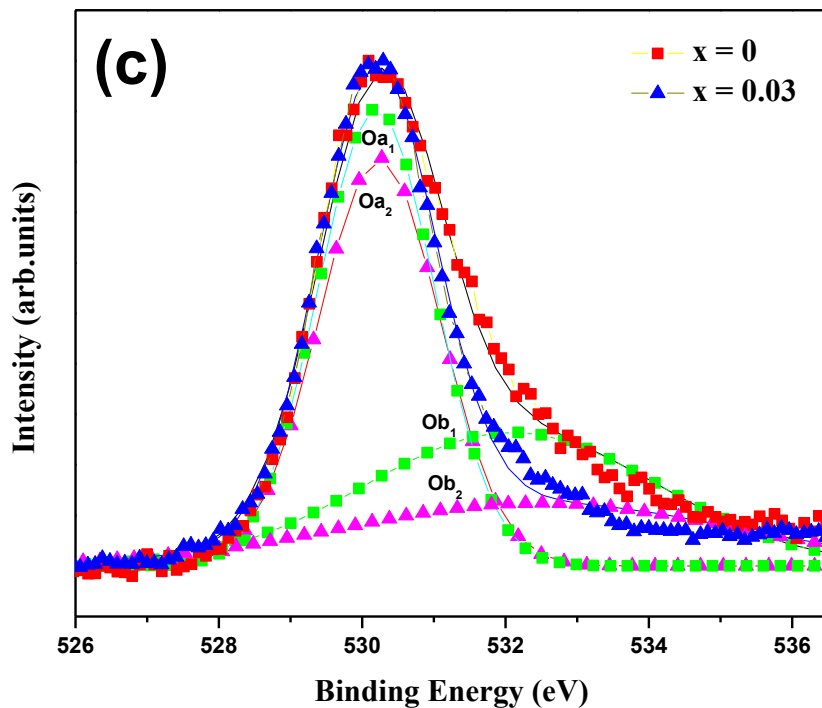
Fig.4.13 XPS core level spectra of (a) Ti 2p, (b) Co 2p (x = 0.03) and (c) O1s of $Ti_{1-x}Co_xO_2$.

4.3 Structural and Magnetic Properties of TiO_2 Nanowires

This section gives the structural, magnetic and charge density distribution studies of anatase TiO_2 nanowires synthesised through two-step hydrothermal reaction route. The detailed synthesis technique is given in Chapter III. To characterize the samples TEM, XRD, FE-SEM and SQUID magnetometer have been used. The charge density distribution studies have been carried out using Maximum Entropy Method (MEM).

4.3.1 Structural Properties of TiO_2 Nanowires

For the synthesis of TiO_2 nanowires (B_1), the corresponding nanoparticles have been synthesised through the hydrothermal technique (sample A_1). The as synthesised nanowires have been calcined at 500 °C for 1h (Sample C)
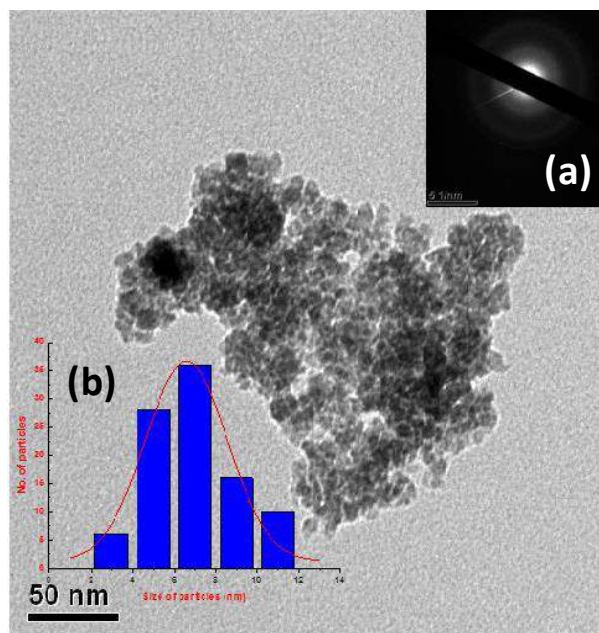
Fig.4.14 TEM micrograph of the as synthesised TiO$_2$ nanoparticles. Inset (*a*) shows the SAED pattern and (*b*) particle size distrubution hisotogram of the nanoparticles.

Fig.4.14 depicts the TEM micrograph of the sample A$_1$. The average particle size is found to be ~ 7 nm as measured from the particle size distribution histogram (inset (*b*) of Fig.4.14). The SAED pattern shows diffused rings suggesting ultrafine particles (inset (*a*) of Fig.4.14). Fig.4.15 (*a*) illustrates the FE-SEM micrograph of sample B$_1$ with low magnification where bundles of nanowires are clearly observed. The nanowires have length of the order of few micrometers and thickness of about 15 nm. The length to thickness ratio clearly indicates the high aspect ratio of these nanowires. When viewed with higher magnification, we find that a single nanowire observed in lower magnified FE-SEM micrograph, in fact, consists of a bunch of nanowires (Fig.4.15 (*a*)). In addition to nanowires, distinct granular particles are also detected as shown in Fig.4.15 (*b*).Under calcination at 500 $^{\circ}$C for 1h (sample C), we observe both the growth of nanowires at the expense of nanoparticles present in sample B$_1$, as well as the disintegration of the bunch of nanowires to few/single nanowire (Fig.4.15 (*c*)) [Du et al. (2003)].
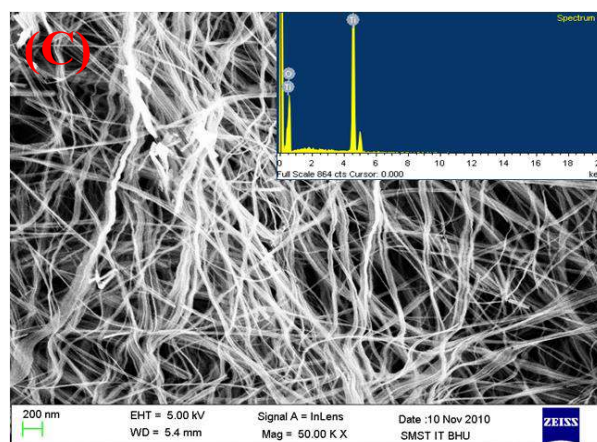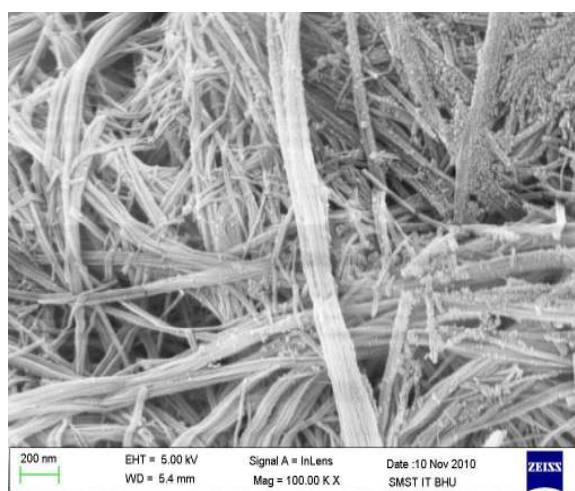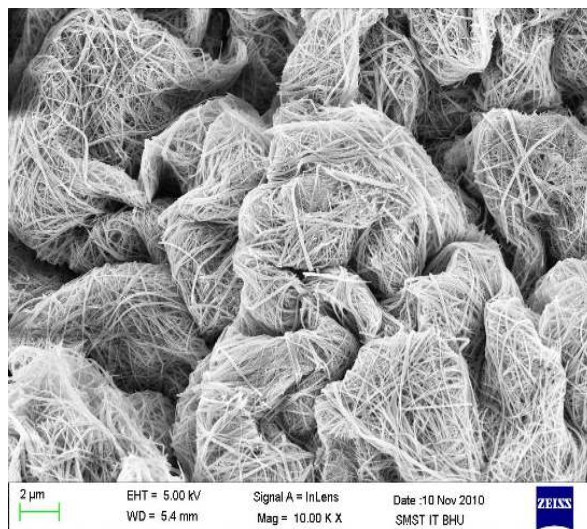
Fig.4.15 FE-SEM: (*a*) low magnification image of sample B$_1$ (*b*) High magnifaction image of sample B (C) High magnification image of sample C (inset shows the EDS spectra of the sample C).
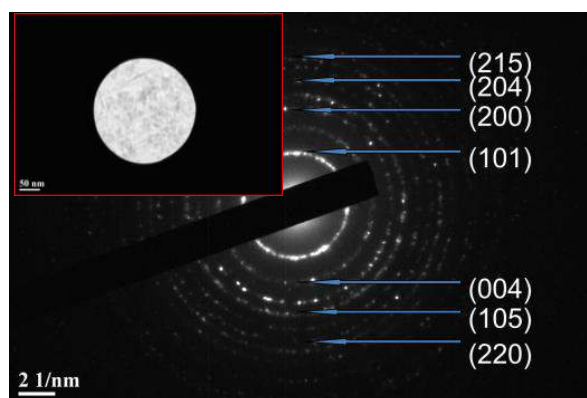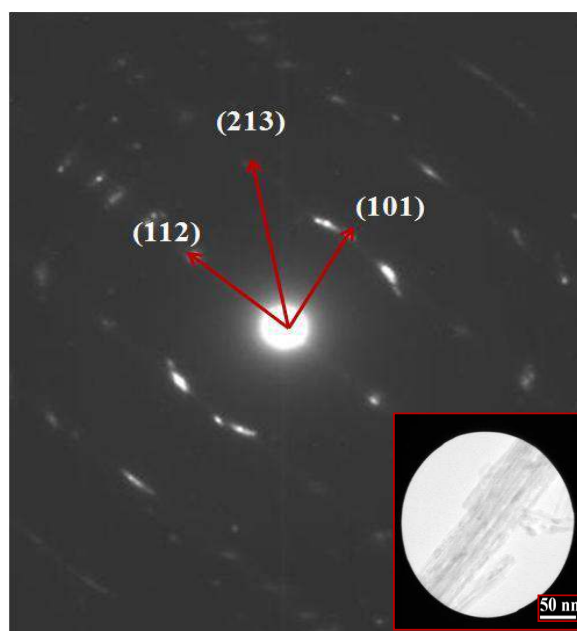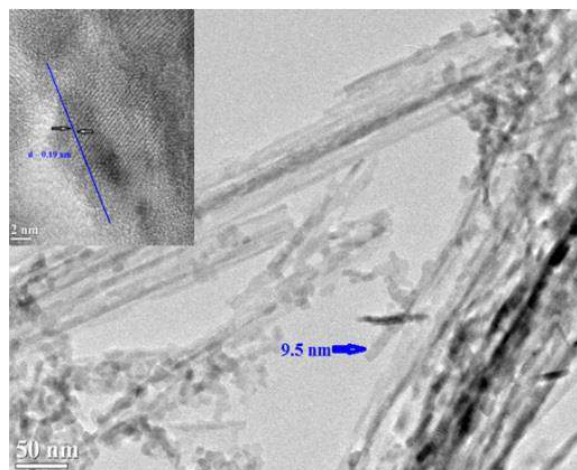
Fig.4.16 (*a*) TEM image of the sample C (inset shows the HREM image of the nanowire) ,(*b*) SAED pattern of the sample C (inset shows the selected bunch of nanowires) and (c) SAED pattern of nanparticles seen in the sample C (inset shows the selected area).

Fig.4.16 (*a*) illustrates a typical TEM micrograph of the sample C revealing bunch of nanowires along with the presence of nanoparticles. The inset of Fig.4.16 (*a*) shows the HREM image of a nanowire with d spacing ~ 1.9 Å related to (200) plane of anatase structure of TiO_2. The SAED pattern of bunch of nanowires clearly shows the distinct diffraction spots indicating the single crystalline nature of the wires (Fig.4.16 (*b*)). The diffraction spots are indexed as (103), (130) and (233) of anatase phase. The slightly diffused and displaced diffraction spots suggest the tilting among the nanowires, the angle of tilting is found to be ~ 20.4^o. TEM clearly indicates the presence of both particles along with the nanowires. Fig.4.16 (c) depicts the SAED pattern of assembly of nanoparticles observed in TEM grid for sample C. Nanowire formation through wet chemical method generally contains many defects which can make them brittle as observed previously [Shim et al. (2010); Han et al. (2010)].We feel that in our case, ultrasonication of samples for half an hour before depositing in TEM grid for measurement may lead to the disintegration of the nanowires to nanoparticles. The nanowires having relatively fewer defects are survived during this process whereas others with higher defects might be broken.

Literatures suggest that the concentration and type of alkali and reaction temperature in hydrothermal process greatly influence the phase and thickness of the one dimensional nanostructure of TiO_2. For example, it has been shown that 10 M NaOH solvent yields nanowires of TiO_2 (B) phase [Armstrong et al. (2004)]. With same solvent, TiO_2 nanotubes of anatase phase have been formed at a reaction temperature of 200 ^{o}C [Wang et al. (2010)]. However, reducing the synthesis temperature to 130 ^{o}C, $H_2Ti_3O_7$ nanotubes are formed using the same concentration of the solvent [Zhang et al. (2005)]. Using 10 M KOH solvent, while Du et al. (2003) report the formation of $K_2Ti_6O_{13}$, Yoshida et al. (2005) end up with titanate phase using 10 M NaOH. Similarly, the thickness of the layered structures depends on reaction temperature maintained in the autoclave. For example, at 110 ^{o}C, the growth of TiO_2 particles are limited and the thickness of the layer is very thin which could be easily rolled up into

tubular structure [Kasuga et al. (1998)]. However, at high reaction temperature like 200 ^{o}C, the thickness of the intermediate layer is thicker that results into nanowires [Zhang et al. (2002)]. Changing the concentration of KOH solvent to 11 M with reaction temperature 130 ^{o}C for 48h duration, Wang et al. (2007) observe nano tubes of anatase phase coexisting with trace of TiO_2 (B) phase calcining the product at 500 ^{o}C. However, Zhang et al. (2002) observe trace of brookite phase with anatase nanowires during the hydrothermal treatment with 10M NaOH at 200 ^{o}C for 24h. Therefore, it is important to identify the phase of the nanowires/nanotubes as well as the presence of undesirable elements like Na in the sample after the hydrothermal treatment. Theoretical studies suggest that surface free energy of anatase TiO_2 microcrystal is smaller than that of rutile phase in case of nanoscale [Banfield (1998)].Hence the anatase phase of the TiO_2 nanowires is expected which is observed in the present case.

For the elemental analysis of sample C, we carried out EDS of the sample C (shown as Fig.4.15 (*c*)). Only Ti and O peaks are observed together with C peak due to the use of carbon tape for sample mounting. Ignoring the possible existence of undetectable elements such as H in the sample, it may be concluded that nanowires are composed of mainly Ti and O. XPS measurements also yields similar results. In addition, it confirms the Ti is in the +4 valence state. No detectable Na was found in sample C from both EDS and XPS as NaOH has been used as solvent. Hence the possible formation of Na_2TiO_6 is ignored [Armstrong et al. (2004)]. Further, XRD and micro Raman measurements are undertaken to confirm the phase of nanowires as indicated from SAED.

Fig.4.17 (a) and (b) depict the XRD profiles for samples A_1 and C. Rietveld refinement method has been used to refine the observed XRD profile
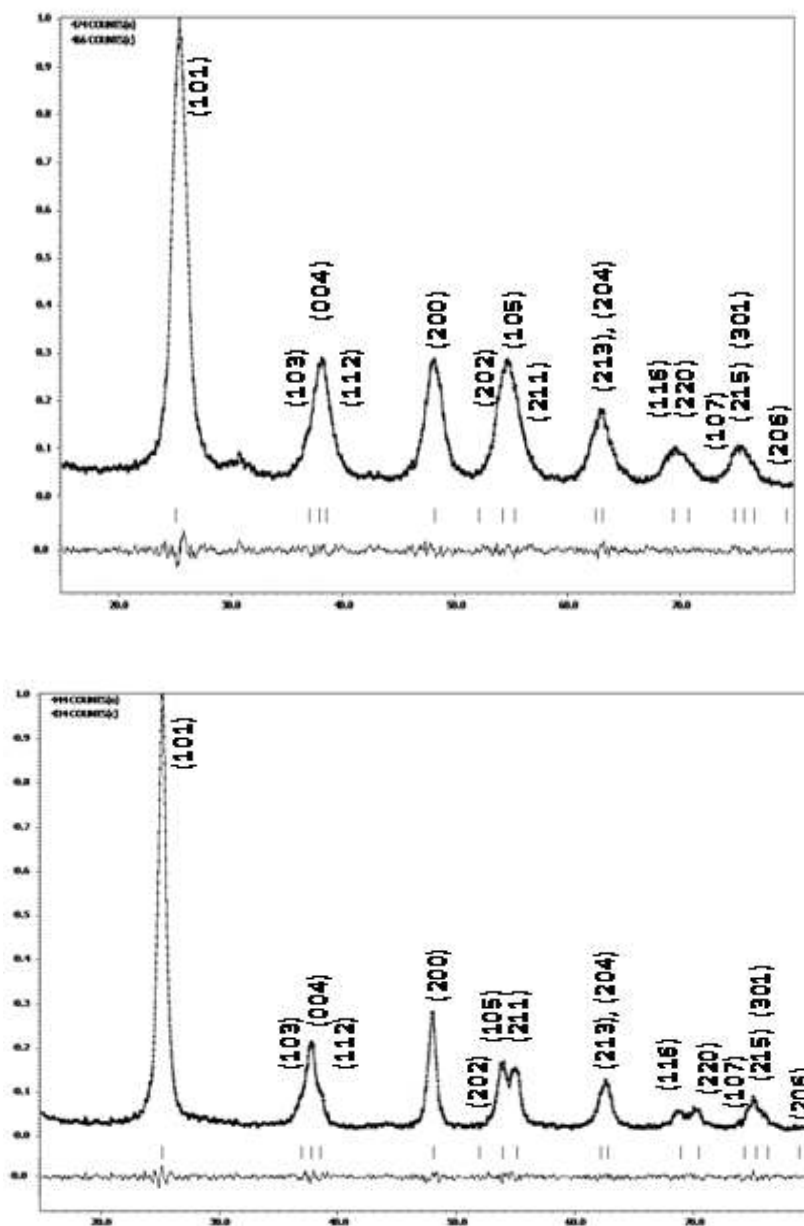
Fig.4.17 Profile fitting for (a) Sample A_1 and (b) Sample C from Rietveld Method.

until it matches well with the calculated profile [Rietveld (1969); McCusker (1999)]. All structural and profile parameters are refined to get an accurate information of the structure using the software package JANA 2006 [Petříček et al. (2006)].The observed and fitted data in Fig.4.17 are shown as dot and line respectively. The lower plot indicates the difference profile between observed and calculated data. Using the space group, I41/amd for anatase structure of TiO_2 and keeping Ti position as (0 0 0), the oxygen position coordinates are

refined and are found to be (0 0 0.202) and (0 0 0.201) for sample A_1 and C respectively. The refined structural parameters are listed in Table 4.2.

Table 4.2 Structural parameters for Sample A_1 and C.

h	k	l	Sample A			Sample C		
			F_o	F_c	$\sigma(F_{obs})$	F_o	F_c	$\sigma(F_{obs})$
1	0	1	61.6827	61.8134	0.6682	61.5148	61.5283	0.6886
1	0	3	20.4507	20.3317	0.2845	21.1734	21.0717	0.3242
0	0	4	75.6087	75.5391	1.0023	77.1711	78.0351	1.0951
1	1	2	28.0999	28.0550	0.3738	27.4419	27.5162	0.4033
2	0	0	90.5271	89.5614	1.1727	92.2253	90.1725	1.3348
1	0	5	57.3102	57.9814	0.7141	57.7053	58.5037	0.8349
2	1	1	41.7518	42.2487	0.5163	41.2836	42.3031	0.5960
2	1	3	18.0712	17.9737	0.2998	19.0417	18.5116	0.3671
2	0	4	55.0065	54.7155	0.9105	58.2646	56.5425	1.1088
1	1	6	49.2315	49.7067	0.7605	47.6564	48.5315	1.0581
2	2	0	64.9607	65.5311	0.9988	65.6473	66.2443	1.4717
1	0	7	16.1455	16.2028	0.2499	15.6338	15.6366	0.3435
2	1	5	43.3563	43.5365	0.6603	43.9819	44.0658	0.8696
3	0	1	32.6182	32.7211	0.4990	33.0325	32.8987	0.6880

The Debye-Waller factor, B_{iso} values for Ti and O atoms are relatively smaller in TiO_2 nanowire than TiO_2 nanoparticles. Possibly the atomic

vibrations are restricted in nanowire and the average thermal vibration parameters are reduced. The cell constants are larger in case of nanowire due to the expansion of lattice planes (Table 4.3).

Table 4.3 Reliable indices from Rietveld analysis.

Parameters	Sample A	Sample C
a (Å)	3.7419(50)	3.7648(18)
c (Å)	9.3682(119)	9.4588(1)
$\alpha = \beta = \gamma$	90	90
Volume(Å^3)	131.2075(3437)	134.0754(1364)
Density(Kg/Å^3)	4.04237(105)	3.9559(40)
Biso (Ti) Å^2	0.6770(1)	0.6481(1)
Biso(O) Å^2	0.7848(1)	0.7486(1)
R (obs)%	0.65	1.34
R_w(obs) %	0.73	1.53
R_p %	4.40	5.85
R_{wp} %	4.86	7.86

This could be possible as high pressure during the hydrothermal synthesis of the nanowires may create such unique changes [Zou et al. (2006)]. Density in case of nanowire is found to be lower than the nanoparticles due to lattice expansion (Table 4.3). The particle size of nanoparticles and nanowires (though it should be single crystalline) are calculated from XRD data using software GRAIN are 7.4587 (2.4794) nm and 11.1389 (2.7323) nm respectively.
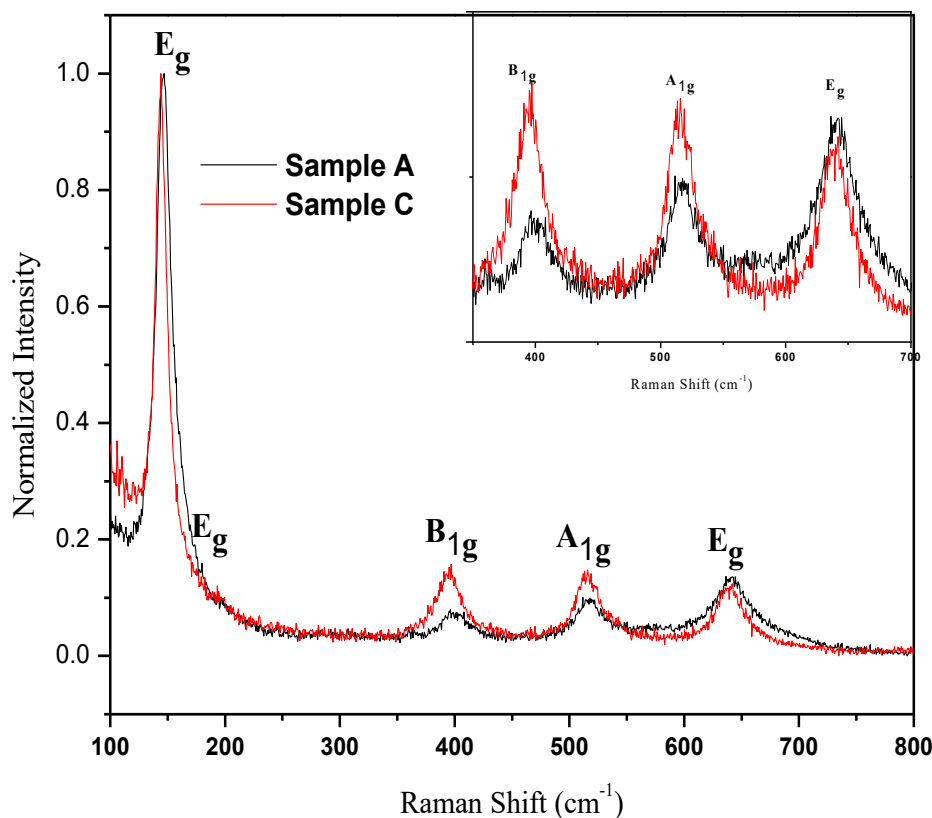
Fig.4.18 Normalized Raman spectra of sample A and C (inset shows the zoomed view).

These values are in good agreement with the average size obtained from TEM results. XRD peak becomes sharper (FWHM decrease) in case of TiO_2 nanowires indicating enhancement in crystallinity than the nanoparticles. Fig.4.18 depicts the normalized Raman spectra of the sample A_1 and Sample C. The observed Raman modes are corroborating well with the six Raman active modes ($A_{1g}+2B_{1g}+3E_g$) of anatase phase of TiO_2 [Ohsaka et al. (1978)].The observed Raman modes are broadened (Fig.4.17), possibly due to quantum confinement effect [Meng et al. (2006)]. The shift of E_g (197 cm^{-1}) mode to low wave number in case of sample C suggests possible stress or quantum confinement effect [Meng et al. (2006); Choi et al. (2005)]. The relative intensities of A_{1g}, B_{1g} and E_g modes in the range 300-700 cm^{-1} is $E_g>A_{1g}>B_{1g}$. But we observe the opposite for the nanowire (sample C) case (inset of

Fig.4.18) which suggests the possible directional behaviour of the wires. We conclude from our microstructural and structural findings that pure anatase nanowires formation could be possible due to two step hydrothermal reaction process which has not been observed before.

4.3.2 Magnetic Properties of TiO$_2$ Nanowires

Magnetisation as a function of temperature for TiO$_2$ nanowires (sample C) under two different probing magnetic fields (500 Oe and 1Tesla) are shown in Fig.4.19. Form the figure it is quite clear that the sample is paramagnetic at 300 K. FC Magnetisation retraces the ZFC curve showing no irreversibility in the case of 1Tesla probing field. However, at 500 Oe probing field a clear irreversibility is seen below 120°C (Fig.4.19 (a)).
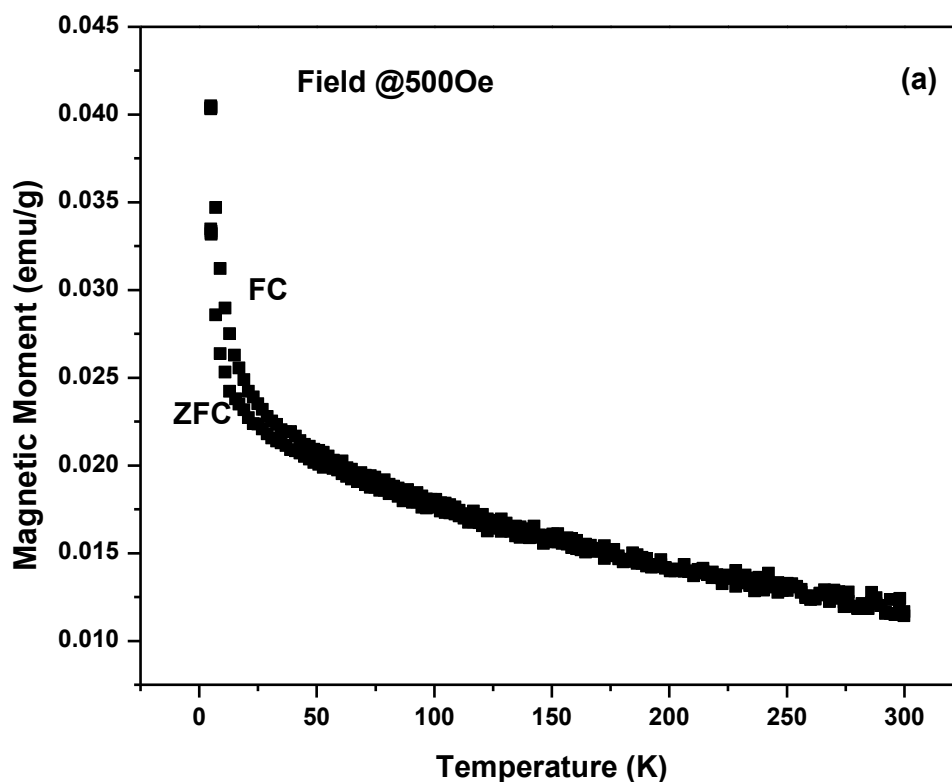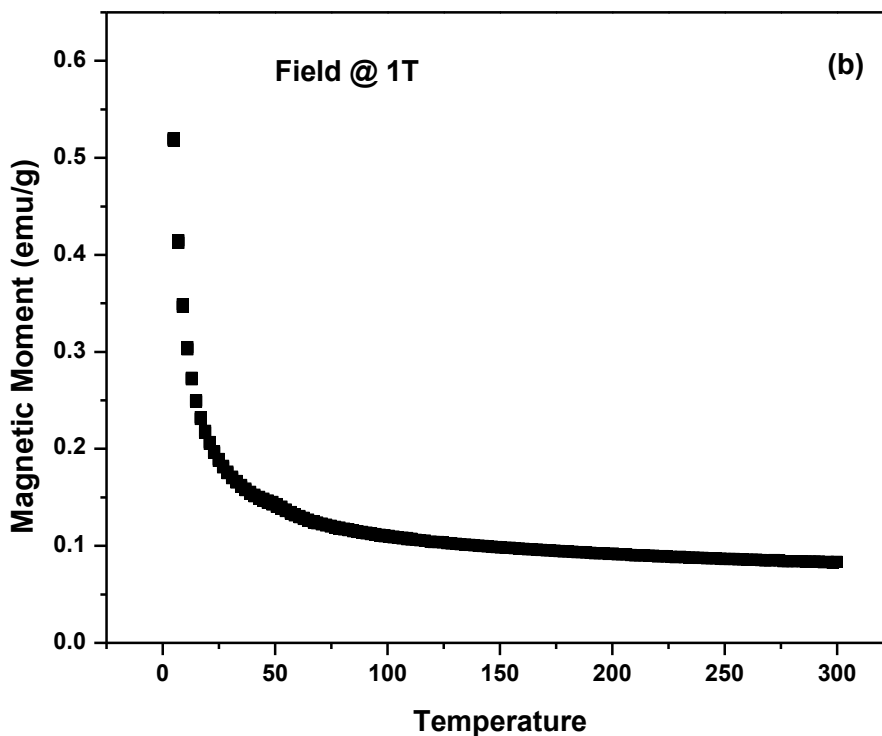
Fig.4.19 Magnetisation (ZFC and FC) as a function of temperature for sample C at a probing field (a) 500 Oe and (b) 1 Tesla.

4.3.3 Charge Density Distribution in Nanoparticles and Nanowires

To understand the nature of chemical bonds precisely, an accurate electron density distribution is indispensible. In this regard, the maximum entropy method is an exact tool to study the electron density distribution because of its resolution. This method is more informative as compared to the conventional Fourier synthesis. In Fourier synthesis method, the electron densities will be biased, due to the series termination error, and negative electron density that prevents clear understanding of bonding between atoms. However, MEM analysis overcomes these problems. The exact electron density distribution would be obtained if all the structure factors were known without ambiguities. However, it is not possible to collect exact values of all the structure factors by x-ray diffraction methods. Number of observable structures
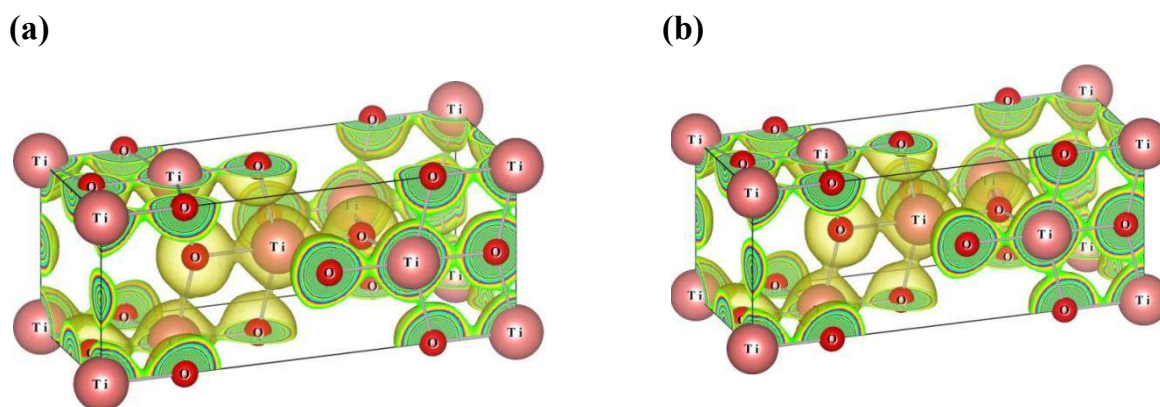
(a)

(b)

Fig.4.20 Three dimensional electron density iso-surface of (a) sample A_1 and (b) sample C.
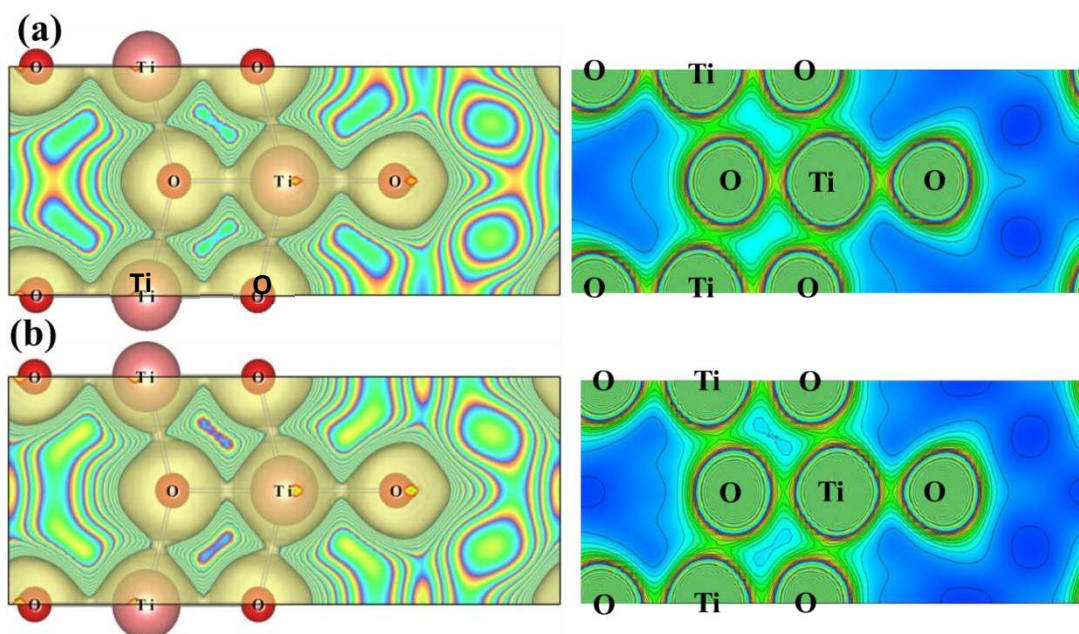

Fig.4.21 Two dimensional electron density distribution of (a) sample A_1 and (b) sample C.

from the experiment is limited and has some errors in them. In view of the information theory, it is not appropriate to use an inverse Fourier transform to construct density distribution owing to a limited number of observed structure factors. There is a finite probability of uncertainties in the results (electron
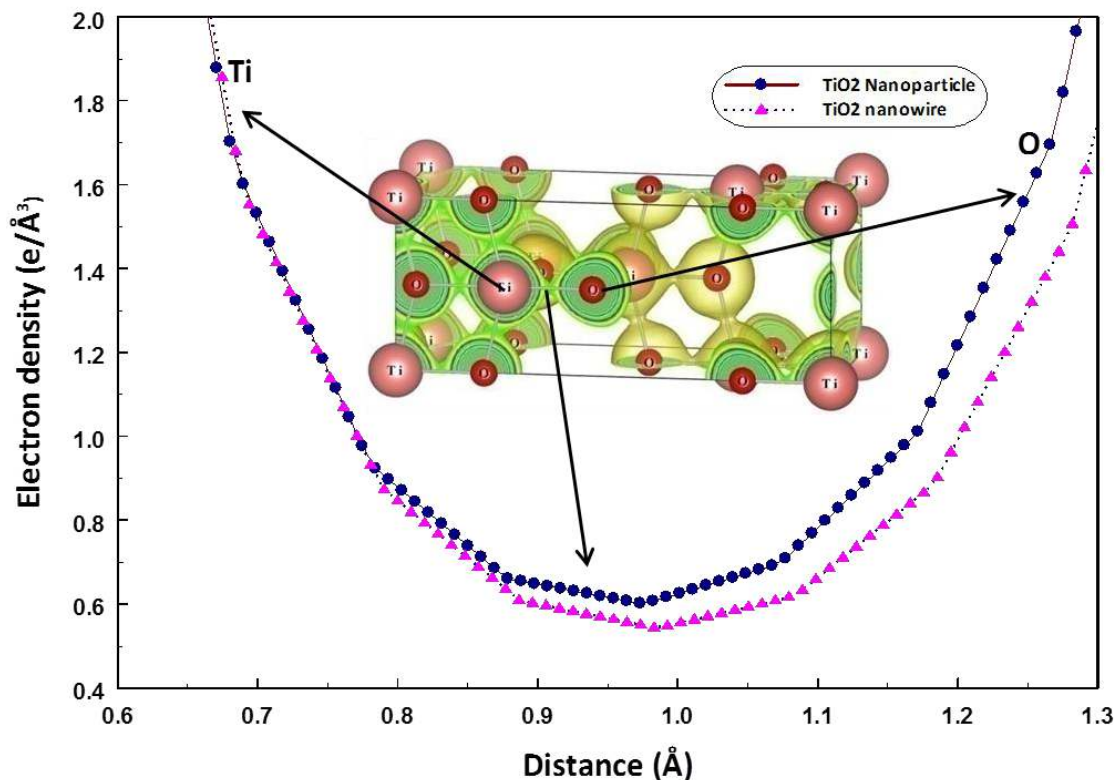
Fig.4.22 One dimensional electron density profile of sample A$_1$ and sample C between Ti and O atoms.

density distribution maps) due to incompleteness of the experimental observations. The MEM is a method that overcomes the aforementioned problem. It is a model free approach in contrast to structure refinements in which the positions of spherical atoms are determined. In this method the concept of entropy is introduced to handle the uncertainty properly. The principle of MEM is to obtain an electron density distribution, which is consistent with the observed structure factors and to leave the uncertainties maximum. MEM was introduced by Gull and Daniel in radio astronomical image processing [Gull and Daniel (1978)]. Collins formulated this method for crystallographic applications [Collin (1982)].Since then MEM has been used as powerful tool to study the electronic structure of the materials. The detailed theoretical calculations are published elsewhere [Bricogne (1988), Yamamoto et al. (1996)].We have used the MEM to construct the charge density distributions around Ti and O atoms in the nanoparticles (sample A$_1$) as well as nanowires (sample C).

Table 4.4 Mid bond electron density between Ti and O atoms.

Parameters	Sample A$_1$	Sample C
Distance from Ti atom (Å)	0.9732	0.9831
Electron Density (e/Å^3)	0.6020	0.5445

The three-dimensional electron density of sample A$_1$ and sample C is drawn in the isosurface level of 0.5 are shown in Fig.4.20 (a) and (b) respectively. Anatase structure of TiO$_2$ is shown with electron density (yellow shade) clouds surrounding Ti and O atoms. The bonding tendency is clearly visualized in two-dimensional electron density contour pictures which are drawn in (010) plane with a distance of 1.87Å from the origin and are shown in Fig.4.21 (a) and (b). In these figures the ionic nature of bond is seen for both samples A$_1$ and C. This behaviour is also inferred in one-dimensional profiles as shown in Fig.4.22. The mid bond electron density in nanowire (sample C) is found to be less than nanoparticles (sample A$_1$) as tabulated in Table 4.4, which suggests more ionic character of nanowires than the nanoparticles. As the one dimensional nanostructure (sample C) is prepared through sintering at 500°C. Due to this temperature effect, the volume of sample C expands, leading to lesser density. Hence the volume of sample C should increase and the mid bond electron density reduces and gets more ionic nature.

4.4 Summary

XRD and Raman spectroscopic studies show that TiO$_2$ samples prepared by the sol-gel technique at *p*H of precipitation 4.5and 6.5 are anatase. After calcining at 800 °C while the sample prepared at *p*H 4.5 shows a mixed anatase and rutile phases, the sample prepared at the *p*H of 6.5 shows a complete rutile phase. At 850 °C, the former sample shows a complete rutile phase C. Such *p*H of precipitation dependent anatase to rutile transformation has not been shown earlier. In addition, we observed a much lower anatase to rutile transformation

temperature ever reported. XPS shows that the oxygen vacancy in the sample prepared at pH 6.5 is higher than the sample prepared at the pH of 4.5. This difference in oxygen vacancy drives the anatase to rutile transformation temperature to a lower value. In case of nanosized anatase $Ti_{1-x}Co_xO_2$ synthesised by a sol-gel technique show no ferromagnetic ordering down to 10K upto x = 0.05. However, magnetic moment in x = 0 is found to be higher than x = 0.01 and 0.03 sample. Higher oxygen vacancy observed in x = 0 shows higher magnetic moment than the sample (x = 0.01 and 0.03) with comparatively lower oxygen vacancy. The synthesised TiO_2 nanowires are found to be single crystalline in nature. From the charge distribution study, it was found that nanowire seems to be more ionic than the nanoparticles.TiO_2 nanowires were found to be paramagnetic at room temperature.